Analysis and Measurement of 3D Torque and Forces for Slotless Permanent Magnet Motors

A. Looser* and T. Baumgartner*
Student Members, IEEE
Power Electronic Systems Laboratory
ETH Zurich
CH-8092 Zurich, Switzerland
looser@lem.ee.ethz.ch, baumgartner@lem.ee.ethz.ch

J.W. Kolar
Fellow, IEEE
Power Electronic Systems Laboratory
ETH Zurich
CH-8092 Zurich, Switzerland
kolar@lem.ee.ethz.ch

C. Zwyssig
Member, IEEE
Celeroton AG
Technoparkstr. 1
CH-8005 Zurich, Switzerland
christof.zwyssig@celeroton.com

Abstract—Slotless windings, both skewed and rhombic, are widely used in industry. In addition to the drive torque, possibly undesirable transverse torques and forces are generated. An analytical derivation of the torque and force components in all three directions is detailed in this paper for the skewed and the rhombic winding. It is shown that for some winding configurations alternating transverse torque components are generated, which may compromise stable operation in applications where for example magnetic or gas bearings are involved. FEM results, which enable the transverse torque for various winding geometries to be quantified, are also included. Finally, the theoretical results are verified by measurements.

Index Terms—Slotless winding, skewed type winding, rhombic winding, 3D torque and forces, permanent magnet machine, BLDC motor

I. INTRODUCTION

Slotless windings are widely used for small-sized electric motors in industrial applications ranging from a hundred milliwatts to a few hundred watts [1]. The main advantages of a slotless design are the absence of cogging torque, the elimination of losses caused by slot space harmonics and the low winding inductance. The last two reasons also make it an excellent choice for high-speed motors [2].

An overview of different types of slotless windings is given in [3] and [4]. The skewed type and the rhombic winding are commonly used types of windings. As can be seen from Figure 1 both windings exhibit complex three-dimensional structures with two overlapping layers. Undesirable transverse torque and force components can be generated in addition to the intended drive torque in the axial direction due to the complex geometry and the obliquely wound strands. Figure 2 illustrates the formation of the drive and the transverse torque considering the Lorentz forces in the winding conductors, which are the reaction forces of a torque generated on the rotor. For a obliquely positioned conductor pair with current I and a permanent magnet field B in the xy-plane, the Lorentz force acting on the conductor possesses a tangential force component F_θ whilst - due to the oblique arrangement of the conductors - an axial force component F_z is also present. The drive torque T_z is generated by the tangential force couple

(a) (b)

Fig. 1. Skewed winding (a) and rhombic winding (b)

F_θ whereas the axial component F_z is responsible for the transverse torque T_{xy}. Depending on the winding type, the geometry and the number of pole-pairs, the transverse torque components of the individual strands within the winding are then superimposed either constructively or destructively.

The unwanted transverse torque and forces generally need to be absorbed by the bearing system. In some high-speed applications where rotor dynamics are crucial, e.g. when magnetic bearings or gas bearings are involved, these transverse torque components have to be either avoided by choosing an appropriate winding type, configuration and geometry or they have to be quantified such that they can be incorporated into the rotor dynamic models. Therefore, estimates for the absolute values as well as models for the time behavior of the transverse torque and forces are needed.

The magnetic field in the air-gap has been studied in [5], [6] and [7], where analytical field descriptions, which are used for the analysis of the torque and force components in this work, were derived. Winding factors of air-gap windings for the harmonic field components resulting in alternating drive torque have been analyzed, e.g. in [4]. However, a comprehensive study of the transverse torque and possible non-vanishing forces for air-gap windings has not been published, thus an initial analysis with measurements for the transverse torque and non-vanishing force components for the skewed winding has been given in [8]. In this work, the analysis is extended and includes an analytical derivation of the 3D torque and force vectors for both the skewed and the rhombic winding. While the analytical derivation based on the integration of the
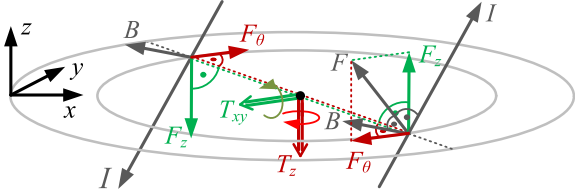
Fig. 2. Lorentz forces for an obliquely arranged conductor pair with current I and a magnetic field in the xy-plane. The tangential force component F_θ yields a drive torque T_z, while the axial component F_z results in a transverse torque T_{xy}.

Lorentz force yields correct results for both drive torque and transverse torque for an iron-less motor design, FEM results that also account for reluctance forces are introduced for the transverse torque in the case of a motor design with a stator back-iron.

The analysis starts with governing equations and assumptions made in Section II followed by a detailed analytical derivation of the torque and force components based on the Lorentz force for the skewed type winding in Section III. In Section IV FEM results accounting for reluctance forces for the skewed type winding are explained. In an abbreviated form, analytical results of the torque and force components of the rhombic winding are given in Section V. Finally, the measurement setup is described in Section VI and measurements verifying the theoretical results are presented.

II. GOVERNING EQUATIONS AND ASSUMPTIONS

The stator reaction force and torque of an electric machine can be calculated by integrating the general force density

$$dF = dF_L + dF_R \tag{1}$$

over the volume of the stator, which can be split up into a Lorentz force component

$$dF_L = J \times B \cdot dV \tag{2}$$

and a reluctance force component

$$dF_R = \frac{1}{2} H^2 \cdot \nabla\mu \cdot dV \tag{3}$$

where J is the current density, B the magnetic flux density, H the magnetic field and $\nabla\mu$ the gradient of the local permeability. The reluctance force density generated on a boundary layer between a high permeability material $\mu \to \infty$ and a material with permeability μ_0 can further be simplified to

$$dF_R = \frac{1}{2\mu_0} B^2 \cdot dA \tag{4}$$

where dF_R and the total flux density B and the normal of the boundary layer surface element dA are collinear. In regions with constant permeability μ the force $dF_R = 0$ vanishes. Using (4) for a slotless motor on the surface of the rotationally

symmetric stator core with inner radius R, the reluctance torque component in axial direction

$$dT_{z,R} = \left(R \frac{dA}{\|dA\|} \right) \times \left(\frac{1}{2\mu_0} B^2 \cdot dA \right) = 0 \tag{5}$$

always vanishes as both factors in the cross product, the distance $R \frac{dA}{\|dA\|}$ and the the force dF_R, are collinear. Hence, for stators studied in this work, analytical calculations for the drive torque T_z using only Lorentz forces and neglecting the reluctance force component yield correct results. However, in order to calculate the transverse torque component, the reluctance term needs to be accounted for.

According to [5] the permanent magnet flux density in the air-gap of a slotless machine can be described in cylindrical coordinates (r, θ, z) by Fourier series for both the radial and the azimuthal field components as

$$B_r = \sum_{n=1}^{\infty} \hat{B}_r^{(n)}(r) \cdot \cos(p(n\theta - \gamma)) \tag{6}$$

$$B_\theta = \sum_{n=1}^{\infty} \hat{B}_\theta^{(n)}(r) \cdot \sin(p(n\theta - \gamma)), \tag{7}$$

where p is the number of pole-pairs of the permanent magnet, γ the permanent magnet orientation angle and $B_r^{(n)}(r)$ and $B_\theta^{(n)}(r)$ are the Fourier coefficients of the nth harmonic. The field in axial direction is assumed to be $B_z = 0$.

It is well known that for machines driven with symmetric sinusoidal currents only the fundamental component of the air-gap field contributes to a constant drive torque. Harmonic field components can yield pulsating drive torque, transverse torque or forces depending on their harmonic order. Therefore, from a design point of view, the flux density of an optimal machine consists solely of the fundamental component. Hence, for the subsequent analysis it is assumed that the geometry of the rotor and the permanent magnets have been ideally chosen such that all the harmonic field components vanish and merely the effects of the winding geometry on the 3D torque and force vectors can be studied. The assumption of a purely fundamental field distribution can be considered realistic as for e.g. a $p = 1$ pole-pair machine, a fundamental field distribution is achieved with the use of cylindrical diametrically magnetized permanent magnet [7]. Omitting all the harmonic components the permanent magnet field in the air-gap can then be written as

$$B_r = \hat{B}_r(r) \cdot \cos(p(\theta - \gamma)) \tag{8}$$
$$B_\theta = \hat{B}_\theta(r) \cdot \sin(p(\theta - \gamma)). \tag{9}$$

A field description in Cartesian coordinates (x, y, z) will be required for the further calculations which yields

$$B = \begin{bmatrix} B_x \\ B_y \\ B_z \end{bmatrix} = \begin{bmatrix} B_r \cdot \cos(\theta) - B_\theta \cdot \sin(\theta) \\ B_r \cdot \sin(\theta) + B_\theta \cdot \cos(\theta) \\ 0 \end{bmatrix}. \tag{10}$$

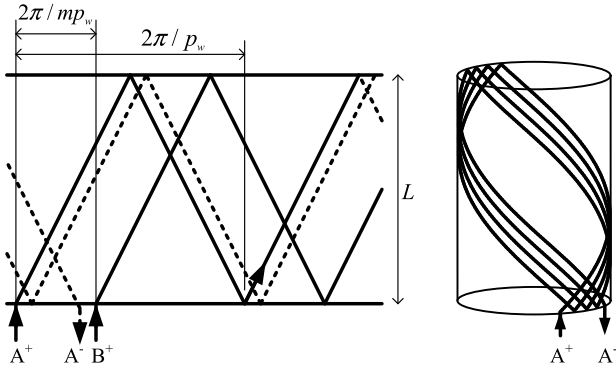Fig. 3.   Winding scheme and 3D structure of the skewed type winding.

Fig. 4.   Coordinate system definition and winding loop parametrization.

III. SKEWED WINDING

In this section, an analytical derivation of the torque and force vectors generated by a skewed winding is given. The derivation is based on the fact, that the reaction torque and force on the rotor are equal to the torque and force generated in the stator. Hence the derivation is based on the integration of the force density over the stator volume. Thereby, the reluctance force caused by the stator core and the armature reaction is intentionally neglected, which allows for a substantial reduction in the complexity of the derivation. Hence only the Lorentz forces generated in the winding are considered. Although the obtained results for the transverse torque are only valid for iron-less motor designs, they still illustrate the qualitative characteristics of the winding. FEM results considering Lorentz and reluctance forces as well as armature reaction giving a quantitative description of the transverse torque are shown in Section IV.

A. Winding Definition

A winding is defined by the number of phases $m \geq 3$ and the number of pole-pairs p. A phase belt spreads over an angle $2\pi/mp$ (Figure 3) for each pole resulting in two consecutive phase belts overlapping. Therefore, consecutive phase belts are arranged in two layers lying on top of each other resulting in a phase asymmetry, which however is not considered in the further analysis.

Different winding description would be necessary for $m = 1$ and $m = 2$. However, as no constant torque can be achieved with a single-phase winding, it is not further considered. The two-phase winding has a very low utilization factor when having only two windings situated $\pi/2$ to each other, because then only half of the volume is used for the winding. The introduction of windings connected in series on the opposite sides in the unused space to overcome this drawback results in a four-phase winding ($m = 4$), which is then covered by the given definition.

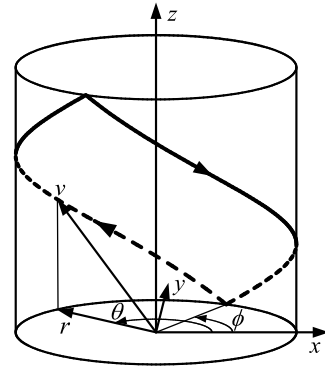A single winding loop starting from angle ϕ as depicted in

Figure 4 can be described by the vector

$$\boldsymbol{v} = \begin{bmatrix} v_x(\theta) \\ v_y(\theta) \\ v_z(\theta) \end{bmatrix} = \begin{bmatrix} r \cdot \cos(\theta) \\ r \cdot \sin(\theta) \\ v_z(\theta) \end{bmatrix} \tag{11}$$

with the z component given by

$$v_z(\theta) = -\frac{L}{2} + \frac{pL}{\pi} \cdot \begin{cases} (\theta - \phi), & \text{for} \quad 0 < \theta - \phi < \frac{\pi}{p} \\ (\frac{2\pi}{p} - \theta + \phi), & \text{for} \quad \frac{\pi}{p} < \theta - \phi < \frac{2\pi}{p} \end{cases} \tag{12}$$

and L being the active length in z direction.

The winding current is defined by a current space vector with phase angle ε. Thus, the current density in the winding loop belonging to the kth phase ($0 \leq k \leq m-1$) conducting a current of phase shift $\varphi_{ph} = 2\pi k/m$ is given by

$$\boldsymbol{J} = J \frac{d\boldsymbol{s}}{\|d\boldsymbol{s}\|} \tag{13}$$

where J is defined as

$$J = \hat{J} \cdot \cos(\varepsilon - \varphi_{ph}) \tag{14}$$

and $d\boldsymbol{s}$ is given by

$$d\boldsymbol{s} = \frac{\partial \boldsymbol{v}}{\partial \theta} d\theta. \tag{15}$$

The calculation of the current density $\hat{J}$ from a given phase current and winding geometry is given in the Appendix.

B. 3D Lorentz Force and Torque

The Lorentz force on an infinitesimal conductor element with volume dV calculated by the triple product

$$dV = |(rd\boldsymbol{\phi} \times d\boldsymbol{r}) \cdot d\boldsymbol{s}| = \frac{pL}{\pi} d\theta r d\phi dr. \tag{16}$$

is given by

$$d\boldsymbol{F} = \boldsymbol{J} \times \boldsymbol{B} \cdot dV = \frac{J \cdot \frac{\partial \boldsymbol{v}}{\partial \theta} \times \boldsymbol{B}}{\sqrt{1 + \left(\frac{\pi r}{pL}\right)^2}} d\theta r d\phi dr \tag{17}$$

The torque generated by that element in respect to the origin is given by

$$d\boldsymbol{T} = \boldsymbol{v} \times d\boldsymbol{F}. \tag{18}$$

The torque and the force generated by a single phase is then obtained by integration over one winding loop and one phase belt and summation over all pole-pairs as

$$\boldsymbol{T}_{ph} = \frac{J}{2} \sum_{h=0}^{p-1} \int_{R_3}^{R_4} \int_{\frac{\varphi_{ph}+2\pi h - \pi/m}{p}}^{\frac{\varphi_{ph}+2\pi h + \pi/m}{p}} \int_{\phi}^{\phi+\frac{2\pi}{p}} \frac{\boldsymbol{v} \times \frac{\partial \boldsymbol{v}}{\partial \theta} \times \boldsymbol{B}}{\sqrt{1+\left(\frac{\pi r}{pL}\right)^2}} d\theta r d\phi dr \tag{19}$$

and

$$\boldsymbol{F}_{ph} = \frac{J}{2} \sum_{h=0}^{p-1} \int_{R_3}^{R_4} \int_{\frac{\varphi_{ph}+2\pi h - \pi/m}{p}}^{\frac{\varphi_{ph}+2\pi h + \pi/m}{p}} \int_{\phi}^{\phi+\frac{2\pi}{p}} \frac{\frac{\partial \boldsymbol{v}}{\partial \theta} \times \boldsymbol{B}}{\sqrt{1+\left(\frac{\pi r}{pL}\right)^2}} d\theta r d\phi dr, \tag{20}$$

where the factor $\frac{1}{2}$ results from the two-layer structure of the winding. Summing-up over all m phases yields the total torque and the total force

$$\boldsymbol{T} = \sum_{k=0}^{m-1} \boldsymbol{T}_{ph} \bigg|_{\varphi_{ph}=\frac{2\pi k}{m}} \tag{21}$$

and

$$\boldsymbol{F} = \sum_{k=0}^{m-1} \boldsymbol{F}_{ph} \bigg|_{\varphi_{ph}=\frac{2\pi k}{m}}. \tag{22}$$

Evaluating (19) and (21) yields the torque

$$\boldsymbol{T} = \begin{bmatrix} T_x \\ T_y \\ \frac{-4m\sin(\frac{\pi}{m})\hat{J}L\sin(\varepsilon-\gamma)}{\pi} \int_{R_3}^{R_4} \frac{\hat{B}_r r^2 dr}{\sqrt{1+\left(\frac{\pi r}{pL}\right)^2}} \end{bmatrix} \tag{23}$$

where for $p=1$ and $m=3$ the transverse torque components are

$$T_x = \frac{3\sqrt{3}\hat{J}L^2 \sin(\varepsilon+\gamma)}{8\pi} \int_{R_3}^{R_4} \frac{\left(\hat{B}_r + \hat{B}_\theta\right) r dr}{\sqrt{1+\left(\frac{\pi r}{p_w L}\right)^2}} \tag{24}$$

and

$$T_y = \frac{3\sqrt{3}\hat{J}L^2 \cos(\varepsilon+\gamma)}{8\pi} \int_{R_3}^{R_4} \frac{\left(\hat{B}_r + \hat{B}_\theta\right) r dr}{\sqrt{1+\left(\frac{\pi r}{pL}\right)^2}}. \tag{25}$$

The transverse torque components vanish ($T_x = T_y = 0$) for $p = 1$ only with even numbers of phases ($m = 4, 6, 8 \ldots$). If $p > 1$, the transverse torque components vanish for any $m > 2$.

Evaluating (20) and (22) yields a vanishing force $\boldsymbol{F} = \boldsymbol{0}$ for any combination of p and m.

C. One-Pole-Pair Three-Phase Winding

The transverse torque components T_x and T_y given by (24) and (25) do not disappear for the one-pole-pair three-phase winding, $p = 1$ and $m = 3$. In order to compare the amplitudes of the drive torque T_z and the transverse torque components T_x and T_y, the integral over the radius needs to be solved and
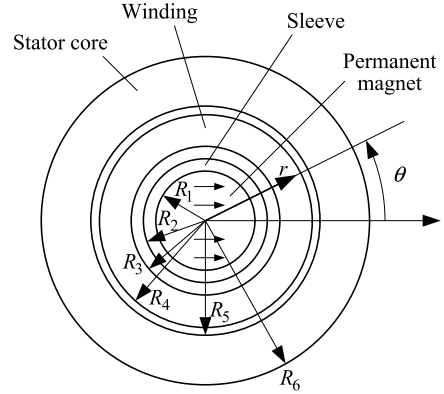

Fig. 5. Machine cross-section and symbol definitions: diametrically magnetized cylindrical permanent magnet rotor inside a slotless stator.

therefore the radial dependency of the flux density has to be considered.

The equations for the flux density $\boldsymbol{B}$ for $p = 1$ are derived in [7] and the machine parameter definitions are given in Figure 5. Simplifying the equations for the radial and azimuthal components of the flux density by setting the relative permeability of the permanent magnet and the stator core $\mu_{r,pm} \approx 1$ respectively $\mu_{r,Fe} \to \infty$ yields

$$\hat{B}_r(r) = \frac{B_{rem}R_1^2}{2R_5^2}\left(\frac{R_5^2}{r^2}+1\right) \tag{26}$$

$$\hat{B}_\theta(r) = \frac{B_{rem}R_1^2}{2R_5^2}\left(\frac{R_5^2}{r^2}-1\right). \tag{27}$$

The torque generated by a three-phase winding ($m = 3$) is obtained by evaluating (23), (24) and (25) to

$$\boldsymbol{T} = \begin{bmatrix} \hat{T}_{xy}\sin(\varepsilon+\gamma) \\ \hat{T}_{xy}\cos(\varepsilon+\gamma) \\ -\hat{T}_z\sin(\varepsilon-\gamma) \end{bmatrix} \tag{28}$$

with

$$\hat{T}_{xy} = \frac{3\sqrt{3}\hat{J}B_{rem}L^2 R_1^2}{32\pi} \cdot K_1 \tag{29}$$

$$\hat{T}_z = \frac{3\sqrt{3}\hat{J}B_{rem}L^2 R_1^2}{4\pi^4} \cdot K_2 \tag{30}$$

where K_1 and K_2 are given by

$$K_1 = \log\left(\frac{L+\sqrt{L^2+\pi^2 R_3^2}}{L+\sqrt{L^2+\pi^2 R_4^2}} \cdot \frac{L-\sqrt{L^2+\pi^2 R_4^2}}{L-\sqrt{L^2+\pi^2 R_3^2}}\right) \tag{31}$$

and

$$K_2 = \frac{1}{R_5^2}\left[\pi R_4 \sqrt{L^2+\pi^2 R_4^2} - \pi R_3 \sqrt{L^2+\pi^2 R_3^2}\right.$$
$$\left. + (2\pi^2 R_5^2 - L^2)\cdot\log\left(\frac{\pi R_4+\sqrt{L^2+\pi^2 R_4^2}}{\pi R_3+\sqrt{L^2+\pi^2 R_3^2}}\right)\right]. \tag{32}$$
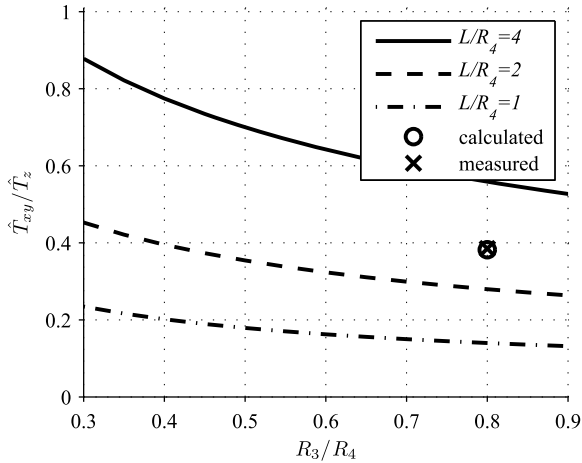
Fig. 6. Ratio of Lorentz transverse torque $\hat{T}_{xy}$ to drive torque $\hat{T}_z$ for the two-pole, three-phase winding without iron stator core ($R_5 \to \infty$) in dependency of the geometry parameters active length L, winding inner radius R_3 and winding outer radius R_4. The calculated value for the experimental winding of Table I is shown with a circle, the measured value with a cross.

Fig. 7. Ratio of total transverse torque $\hat{T}_{xy}$ to drive torque $\hat{T}_z$ for the two-pole, three-phase winding with an iron stator core in dependency of the geometry parameters active length L, winding inner radius R_3 and winding outer radius $R_4 = R_5$. The calculated value for the experimental winding of Table I is shown with a circle, the measured value with a cross.

In order to produce a constant and maximum drive torque the angle between the current space vector ε and the rotor orientation γ needs to be $\varepsilon - \gamma = -\pi/2$. For a motor rotating with a rotational speed Ω, i.e. $\gamma = \Omega t$ and $\varepsilon = \Omega t - \pi/2$ the transverse torque then alternates with a frequency of twice the rotational speed 2Ω.

As mentioned above, (28)-(32) are based on the Lorentz forces generated within the winding and additional contributions such as reluctance forces caused by the stator core or armature reaction are disregarded. While the effect of the reluctance force is significant, the influence of armature reaction is minor. As known from (5) the result obtained for the drive torque T_z remains unaffected when incorporating the reluctance forces and can therefore be used to analytically calculate the machine's drive torque. However, the results for the transverse torque T_x and T_y are only valid for iron-less motor designs, i.e. for $R_5 \to \infty$. Thus, for the verification of the theoretical results, the torque for an iron-less design is measured in Section VI. (28)-(31) remain unchanged for the iron-less machine and K_2 is given by

$$\lim_{R_5 \to \infty} K_2 = 2\pi^2 \log \left(\frac{\pi R_4 + \sqrt{L^2 + \pi^2 R_4^2}}{\pi R_3 + \sqrt{L^2 + \pi^2 R_3^2}} \right). \tag{33}$$

The ratio of transverse torque to drive torque $\hat{T}_{xy}/\hat{T}_z$ is plotted in Figure 6. It can be seen that high ratios of L/R_4, i.e. long windings, and small ratios of R_3/R_4, i.e. thick-walled windings, result in relatively high transverse torque. This is rather unfavorable as the winding length is usually larger than its outer diameter for common machines and therefore a relatively high amount of transverse torque must be expected.

IV. 3D FEM CALCULATION FOR THE ONE-POLE-PAIR THREE-PHASE SKEWED WINDING

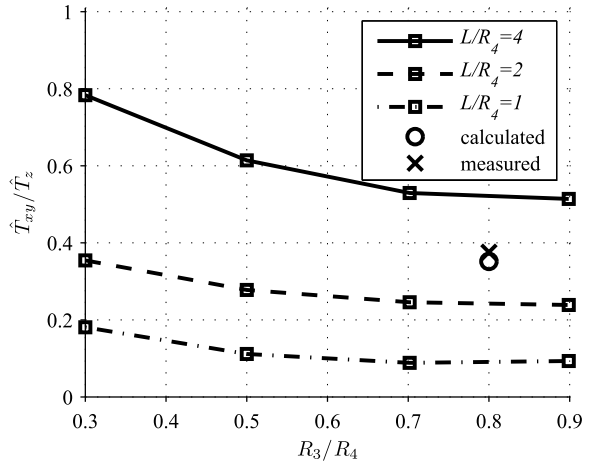In order to determine the transverse torque for machines with an iron stator core, reluctance forces also need to be considered. Therefore a magnetostatic FEM calculation is used to determine the magnetic field generated by the winding.

The flux density caused by a single phase belt is calculated using the commercial FEM software Comsol. Thereby, the cylindrical stator core is modeled as a linear material with a relative permeability $\mu_r = 1000$. The resulting field distribution for the single phase belt is then further used to obtain the total winding field of all three phase belts by superposition.

The total flux density in the motor is given by the superposition of the winding flux density and the flux density caused by the permanent magnet for which again the analytical 2D model from [7] is used. The force and torque is then obtained by numerical integration of the Maxwell Stress Tensor evaluated for the total flux density on the cylindrical surface with radius R_2.

The FEM calculation yields $\boldsymbol{F} = \boldsymbol{0}$ for the force. The FEM results for ratio of transverse torque to drive torque $\hat{T}_{xy}/\hat{T}_z$ are shown in Figure 7. The ratios obtained from FEM calculations and the ratios given by the analytical model are qualitatively very similar: long and thick-walled windings result in high transverse torque. Therefore, a transverse torque in the order of 30% to 40% of the drive torque or more needs to be expected for most machine designs with skewed windings.

V. RHOMBIC WINDING

In this section the force and torque vectors produced by the rhombic winding are analyzed. The analytical derivation is again based on an evaluation of solely the Lorentz forces within the winding, neglecting both reluctance forces and armature reaction. As the analysis can be conducted in a similar way as in Section III, it is presented in an abbreviated form.

The winding scheme of the rhombic winding is shown in Figure 8 for a single phase and pole-pair. Each phase consists of two, series connected, coils sides per pole-pair (A_1 and A_2
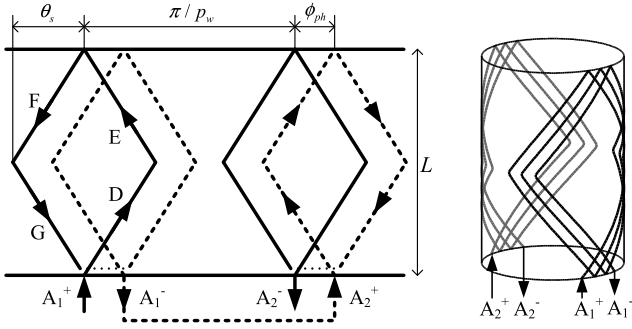
Fig. 8. Winding scheme and 3D structure of the rhombic winding.

Fig. 9. Winding test bench with the stator mounted on the piezoelectric load cell and the permanent magnet fixed to the positioning stage.

for phase A). A single winding loop exhibits the shape of a rhombus, which is divided into loop segments for each side denoted with the letters D, E, F and G.

The winding loop starting from angle ϕ can then be again described by the vector $\boldsymbol{v}$ as defined in (11) however with the z-component redefined as

$$
v_z(\theta) = \frac{L}{2} \cdot \begin{cases} (-1 + \frac{\theta - \phi}{\theta_s}), & \text{for Segment D} \\ (1 - \frac{\theta - \phi}{\theta_s}), & \text{for Segment E} \\ (1 + \frac{\theta - \phi}{\theta_s}), & \text{for Segment F} \\ (-1 - \frac{\theta - \phi}{\theta_s}), & \text{for Segment G} \end{cases} \quad (34)
$$

where θ_s is the winding opening angle, ϕ_{ph} the phase belt width and L the active length in axial direction.

The force and torque vectors generated by the rhombic winding are then calculated similarly to (13)-(22). The force $\boldsymbol{F} = \boldsymbol{0}$ vanishes and the torque is

$$
\boldsymbol{T} = \begin{bmatrix} 0 \\ 0 \\ -\hat{T}_z \cdot sin(\varepsilon - p_w\gamma) \end{bmatrix} \quad (35)
$$

with

$$
\hat{T}_z = 2L\hat{J}m \frac{1 - \cos(p_w\theta_s)}{p_w\theta_s} \sin(\frac{p_w\phi_{ph}}{2}) \int_{R_3}^{R_4} \frac{\hat{B}_r r^2 dr}{\sqrt{1 + \left(\frac{2\theta_s r}{L}\right)^2}}. \quad (36)
$$

Note that, contrary to the skewed winding, the transverse torque components T_x and T_y disappear for the rhombic winding also for $p = 1$ and only a drive torque T_z is produced.

VI. Measurements

A. Measurement Setup

The measurements are performed on a granite measurement platform. The permanent magnet is mounted on a rotational stage. The stator is mounted on a multi component load cell to measure the winding reaction force and torque components resulting from the injected winding currents. A photograph of the described assembly is shown in Figure 9.

A Spitzenberger&Spies DM3000 power supply is used to generate the three-phase symmetric sinusoidal currents fed to the star connected winding at a frequency of 1 Hz. The three-phase currents are measured with current sensors (LEM LTS
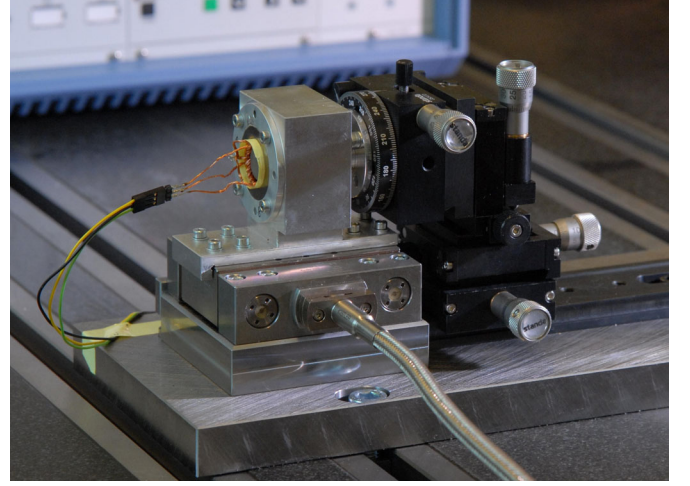
6-NP). The current sensor output signals and force signals are acquired by a National Instruments LabVIEW card at a sample rate of 1 kHz.

The motor windings to be measured are expected to deliver a nominal drive torque of 28.8 Nmm for the skewed winding and 38 Nmm for the rhombic winding. In order to measure such small quantities a piezoelectric multi-component dynamometer (Kistler 9256C1) is used, providing six force measurements in pairs F_{x1} and F_{x2}, F_{y1} and F_{y2} and F_{z1} and F_{z2}, and thereby permitting computation of the resulting forces as well as two of the three torque components. The force components are $F_x = F_{x1} + F_{x2}$, $F_y = F_{y1} + F_{y2}$ and $F_z = F_{z1} + F_{z2}$ and the two torque components are $T_y = a \cdot (F_{x1} - F_{x2}) + b \cdot (F_{z1} - F_{z2})$ and $T_z = c \cdot (F_{y1} - F_{y2}) + d \cdot F_x$, where the term $d \cdot F_x$ accounts for the coordinate transformation from the sensor to the stator coordinate system $(x, y, z) \rightarrow (x, y + d, z)$. a, b and c result from the load cell geometry. The measurements are repeated for the winding rotated by an angle of $90°$ to obtain the torque T_x.

A Kistler type 5017 multichannel charge amplifier is used. The amplifier's internal second order low-pass filters are used and the cut-off frequency is set to 300 Hz for all the measurements.

In respect of amplitude, the forces and torques to be measured are at the lower end of the measurement range of the dynamometer. Hence, precursory quasi-static measurements with test forces applied by a dial gauge and test weights were performed to verify the correct behavior of the load cell. It was concluded that the resulting forces and the torque T_y were measured with high precision, while the torque T_z was deviating 30% and a recalibration based on the applied test forces was needed.

As the generated charge produced by the small forces is low and the charge amplifier operates with high gain, signal drifting needs to be compensated. It is common in piezoelectric force measurements that drift compensation is
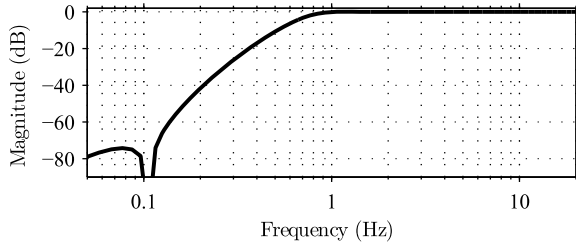
Fig. 10. Frequency response of the drift compensation FIR filter with an attenuation of 0.06 dB at 1.0 Hz.
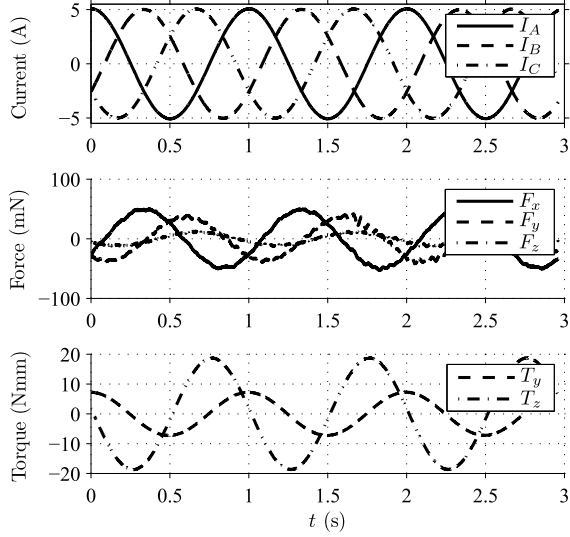

Fig. 11. Measurement of stator reaction torque and forces for a skewed test winding with an iron-less stator core ($R_5 \to \infty$) for rotor position $\gamma = 0$ and current phase $\varepsilon = \Omega t$. The geometric data of the test motor is given in Table I.

made manually by subtracting a linear approximation of the drift considering the beginning and the end of the measurement when no forces are applied. The resulting force and torque components are supposed to be offset-free for symmetric sinusoidal three-phase currents. This simplifies drift compensation and the measured data can be processed off-line through a FIR high-pass filter thereby eliminating the frequency components below 1 Hz. The frequency response of the applied drift compensation filter is shown in Figure 10.

B. Skewed Winding and Iron-Less Design

The geometric data for the $p = 1$ test motor is listed in Table I. In order to allow for measurements without reluctance forces an iron-less design is used. Sinusoidal three-phase currents are injected with $\varepsilon = \Omega t$ such that the resulting stator field rotates in mathematically positive direction. Figure 11 shows the measured force and torque components for the fixed rotor position $\gamma = 0$ after signal drift compensation. Measurements are repeated for rotor positions in steps of $10°$. Another series of measurements is required to obtain the torque component T_x by turning the winding on the measurement setup by $90°$. Figure 12 shows the combined resulting
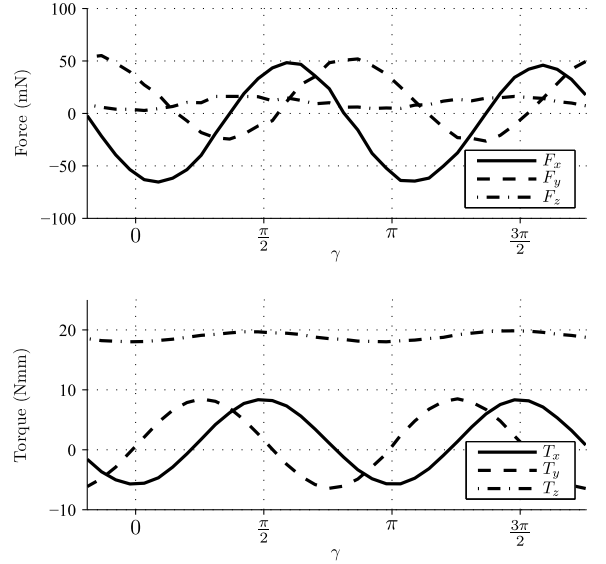

Fig. 12. Combined measured torque and forces for a skewed test winding with an iron-less stator core ($R_5 \to \infty$) for $\varepsilon - \gamma = -\pi/2$. The geometric data of the test motor is given in Table I.
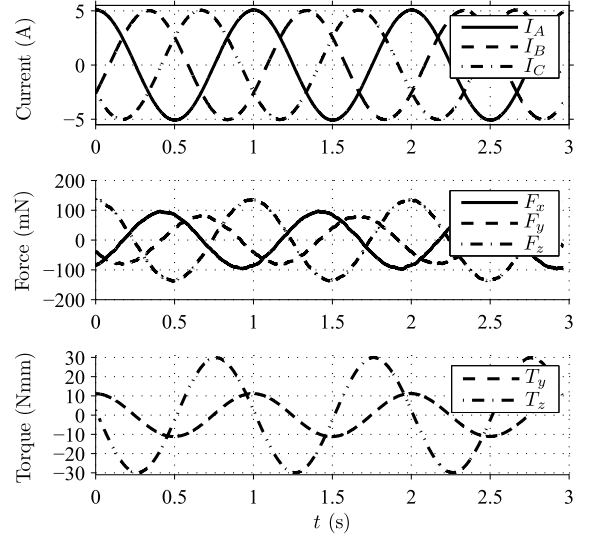

Fig. 13. Measurement of stator reaction torque and forces for a skewed test winding mounted in a iron stator core with an inner radius $R_5 = R_4 = 10$ mm and an outer radius $R_6 = 15$ mm for rotor position $\gamma = 0$ and current phase $\varepsilon = \Omega t$. The geometric data of the test motor is given in Table I.

force and torque components from these measurements for $\varepsilon - \gamma = -\pi/2$, where the maximum drive torque is generated. It can be seen that the transverse torque alternates twice within one rotation, i.e. with twice the rotational frequency. The ratio of transverse torque to drive torque is expected to be $\hat{T}_{xy}/\hat{T}_z = 0.382$ according to analytical calculation, which is in correlation with the measurement that give a ratio of 0.385 (see Figure 6). However, the force components do not disappear completely. The remaining forces make up to 10% of the torque producing differential forces in the sensor. A
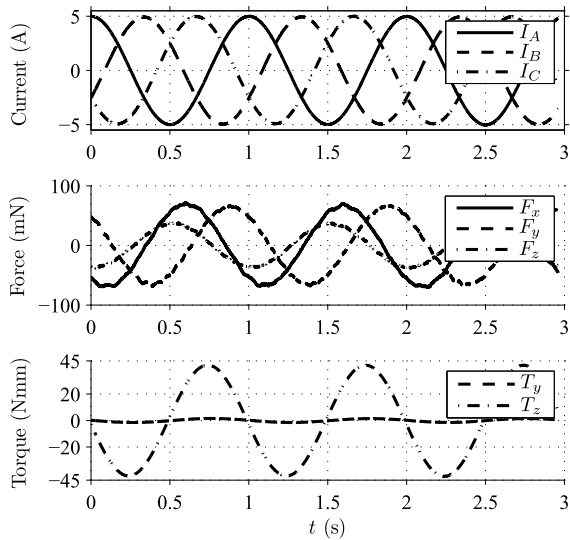
Fig. 14. Measurement of stator reaction torque and forces for a rhombic test winding with an iron stator for rotor position $\gamma = 0$ and current phase $\varepsilon = \Omega t$. The geometric data of the test motor is given in Table II.

small pulsation of the drive torque T_z is also observed. These discrepancies cannot result from non-symmetric currents, as the current measurement error is smaller than 1% and the amplitude deviation of the injected currents was less than 1%. The errors may however be caused by the two layer structure and the associated winding asymmetries, misalignment of rotor and winding or harmonic distortion of the permanent magnet field, which have not been taken into account in the modeling above.

C. Skewed Winding with Iron Stator Core

The measurement shown in the previous section are repeated with a cobalt iron stator core having an inner radius $R_5 = R_4 = 10$ mm and an outer radius $R_6 = 15$ mm. The geometric data is listed in Table I. Figure 13 shows the measured force and torque components for $\varepsilon = \Omega t$ and the fixed rotor position $\gamma = 0$ after signal drift compensation. The measurement shows a drive torque amplitude of $\hat{T}_z = 29.8$ Nmm which is in agreement to the calculated value of 28.8 Nmm. The measured transverse torque amplitude is $\hat{T}_{xy} = 11.2$ Nmm whereas from the FEM calculation a value of 10.1 Nmm was expected. The measured ratio $\hat{T}_{xy}/\hat{T}_z = 0.37$ and the calculated ratio $\hat{T}_{xy}/\hat{T}_z = 0.35$ are drawn in Figure 7.

D. Rhombic Winding

The measurement result of the rhombic one-pole-pair test winding with the geometry data given in Table II for a fixed rotor position $\gamma = 0$ and a rotating current vector is shown in Figure 14. A drive torque of $\hat{T}_z = 38.0$ Nmm is obtained from the calculation whereas $\hat{T}_z = 41.8$ Nmm were measured. Furthermore it is expected that no transverse torque components T_x and T_y are generated in a rhombic winding. Indeed, a very small transverse torque of only 1.5 Nmm was measured. A smoother drive torque T_z with much lower

pulsation compared to the skewed winding was measured for a constant angle $\varepsilon - \gamma = -\pi/2$, which may be a merit of the highly symmetric winding structure.

VII. CONCLUSION

Slotless windings, both skewed and rhombic, are widely used in industrial motor applications. Despite their popularity, their peculiarity of producing transverse torque components in addition to the drive torque seems not to be well known. Unwanted forces and transverse torque generally need to be absorbed by the bearing system. Thus, when rotor dynamics are of concern, e.g. when magnetic or gas bearings are involved, a thorough evaluation of the winding behavior is crucial. Therefore, a qualitative description of the force and torque vectors is derived analytically based on the integration of Lorentz forces within the winding. In order to quantitatively estimate the amount of transverse torque, FEM calculations are shown which also include the reluctance forces which need to be considered when an iron stator core is present. The calculations show, that for some configurations using skewed windings transverse torque can occur. Measurements verify the existence of transverse torques for the one-pole-pair skewed winding, which alternates with twice the frequency of the rotational speed. The calculations show that no transverse torque is generated by the rhombic winding. This has also been verified by measurements.

APPENDIX

The current density amplitude for skewed winding is given by

$$\hat{J} = \frac{N\hat{i}}{A_\perp} \tag{37}$$

where N is the number of winding turns per phase, $\hat{i}$ the phase current amplitude and $A_\perp$ the phase belt area perpendicular

to $d\boldsymbol{s}$, which is calculated by the integral

$$A_\perp = \frac{1}{2} \int_{R_3}^{R_4} \int_{\frac{-\pi}{mp}}^{\frac{\pi}{mp}} \frac{dV}{\|d\boldsymbol{s}\|} = \frac{1}{2} \int_{R_3}^{R_4} \int_{\frac{-\pi}{mp}}^{\frac{\pi}{mp}} \frac{1}{\sqrt{1 + \left(\frac{\pi r}{pL}\right)^2}} r\, d\phi\, dr \quad (38)$$

$$A_\perp = \frac{L}{\pi m} \left(\sqrt{p^2 L^2 + \pi^2 R_4^2} - \sqrt{p^2 L^2 + \pi^2 R_3^2} \right) \quad (39)$$

where the factor $\frac{1}{2}$ results from the two-layer structure of the winding and dV is the volume of an infinitesimal conductor element given in (16).

ACKNOWLEDGMENTS

REFERENCES

[1] U. Kafader and J. Schulze, "Similarity relations in electromagnetic motors - limitations and consequences for the design of small DC motors," in *Proceedings of 9th International Conference on New Actuators (ACTUATOR '04)*, 2004, pp. 309–312.

[2] N. Bianchi, S. Bolognani, and F. Luise, "Potentials and limits of high-speed PM motors," *IEEE Transactions on Industry Applications*, vol. 40, no. 6, pp. 1570 – 1578, Nov.-Dec. 2004.

[3] M. Nagrial, J. Rizk, and A. Hellany, "Design and performance of permanent magnet slotless machines," in *Proceedings of 18th International Conference on Electrical Machines (ICEM 2008)*, Sept. 2008.

[4] B. Hagemann, "Entwicklung von Permanentmagnet-Mikromotoren mit Luftspaltwicklung," Ph.D. dissertation, University Hannover, Germany, 1998.

[5] K. Sridhar, "Electromagnetic models for slotless PM synchronous motor drives," in *Proceedings of Applied Power Electronics Conference and Exposition (APEC '95)*, March 1995, pp. 367–377 vol.1.

[6] M. Markovic and Y. Perriard, "Simplified design methodology for a slotless brushless dc motor," *IEEE Transactions on Magnetics*, vol. 42, no. 12, pp. 3842–3846, Dec. 2006.

[7] J. Luomi, C. Zwyssig, A. Looser, and J. Kolar, "Efficiency optimization of a 100-W 500 000-r/min permanent-magnet machine including air-friction losses," *IEEE Transactions on Industry Applications*, vol. 45, no. 4, pp. 1368 –1377, July-Aug. 2009.

[8] A. Looser, T. Baumgartner, C. Zwyssig, and J. Kolar, "Analysis and measurement of 3D torque and forces for permanent magnet motors with slotless windings," in *Proceedings of IEEE Energy Conversion Congress and Exposition (ECCE 2010)*, Sept. 2010, pp. 3792 –3797.